

Morphy: A Compliant and Morphologically Aware Flying Robot

Paolo De Petris, Morten Nissov, and Kostas Alexis*

This study introduces a novel compliant and morphologically aware aerial robot called Morphy. The system is small (primary dimension 25.2 cm), lightweight (260 g), and agile (thrust-to-weight ratio of 3.3) while simultaneously integrating sensorized flexible joints in its arms. These elastic joints unlock the potential of experiencing flexible deformations, thus enabling the robot to resiliently withstand collisions at high speeds and squeeze through openings more narrow than its nominal dimensions. Extensive analysis of the flexible joints' behavior under static loads and in free flight is conducted. Driven by the deformations that the robot can experience, adaptive control allocation exploiting real-time angle deflection feedback from Hall-effect sensors embedded in the joints is proposed and combined with fixed-gain control. To demonstrate Morphy's performance, multiple experiments are conducted, including free flight trajectory tracking, impacts with the environment, and flying through narrow passages. As shown, the system can withstand collisions up to 7.6 m s^{-1} in drop tests and 3 m s^{-1} midflight while recovering back to hover. Finally, Morphy's capability to passively change its shape and squeeze through openings smaller than its nominal size is showcased both in the horizontal and in the vertical directions.

1. Introduction

The field of aerial robotics and especially rotorcrafts has made significant strides in recent years, particularly with the development of multirotors. Modern flying systems can move quickly and smoothly, with precise control and the ability to execute complex trajectories while navigating around obstacles. However, the overwhelming majority of multirotors are still built with rigid structures, limiting their ability to physically interact with their environment and adapt to their surroundings. This lack of flexibility or morphological adaptation can impact their overall resilience and operational versatility.

P. De Petris, M. Nissov, K. Alexis
Autonomous Robots Lab
Department of Engineering Cybernetics
Norwegian University of Science and Technology
O.S. Bragstads Plass 2D, Trondheim 7034, Norway
E-mail: konstantinos.alexis@ntnu.no

 The ORCID identification number(s) for the author(s) of this article can be found under <https://doi.org/10.1002/aisy.202400493>.

© 2024 The Author(s). Advanced Intelligent Systems published by Wiley-VCH GmbH. This is an open access article under the terms of the Creative Commons Attribution License, which permits use, distribution and reproduction in any medium, provided the original work is properly cited.

DOI: [10.1002/aisy.202400493](https://doi.org/10.1002/aisy.202400493)

The ability to withstand collisions and adapt one's morphology is a crucial trait observed in the majority of flying species in nature. This trait is intrinsically linked to their body structure, which often incorporates flexible and resilient components. For example, studies on the wings of honeybees have highlighted the importance of resilin, an elastomeric protein extensively distributed throughout their wings, which plays a significant role in minimizing damage during collisions and enhancing overall wing durability.^[1] Similar examples demonstrating the importance of embedded soft components can be found in wasps and bumblebees.^[2] Furthermore, research on birds pointed out the importance of safe collisions in flight and the ability to navigate tight gaps smaller than a bird's nominal dimensions. For instance, ref. [3] studied birds flying through gaps with widths ranging from larger than their wingspan to as narrow as one-quarter of their wingspan, while ref. [4] provided insights

into how hummingbirds negotiate smaller openings using a ballistic trajectory characterized by tucked, nonflapping wings.

Inspired by these observations, researchers have begun exploring the integration of flexible components into small flying robots, such as in certain collision-tolerant microaerial vehicle (CT-MAV)s.^[5] Incorporating soft components into the framework of multirotor airframes introduces a previously unexplored level of adaptability, enabling these flying machines to navigate demanding environments with unparalleled resilience. For instance, soft aerial robots can exhibit robust behaviors during high-speed collisions with their surroundings.^[6,7] Their inherent softness also facilitates passive shape morphing, potentially allowing them to maneuver through passages more narrow than their nominal cross section.^[8]

Motivated by the above and leveraging recent advancements of materials and adaptive manufacturing technologies, this study introduces a novel morphologically aware flying robot, named Morphy. The system presents small dimensions (primary dimension 25.2 cm), lightweight structure (260 g), and high agility (thrust-to-weight ratio of 3.3). The design features flexible joints on its arms as depicted in Figure 1, the characteristics of which were analyzed during both free flight and collisions. Inside each flexible joint the platform integrates a 3D Hall-effect sensor, from the measurements of which information about the joint deflection is derived. Exploiting this information, we then develop an adaptation to the standard quadrotor control

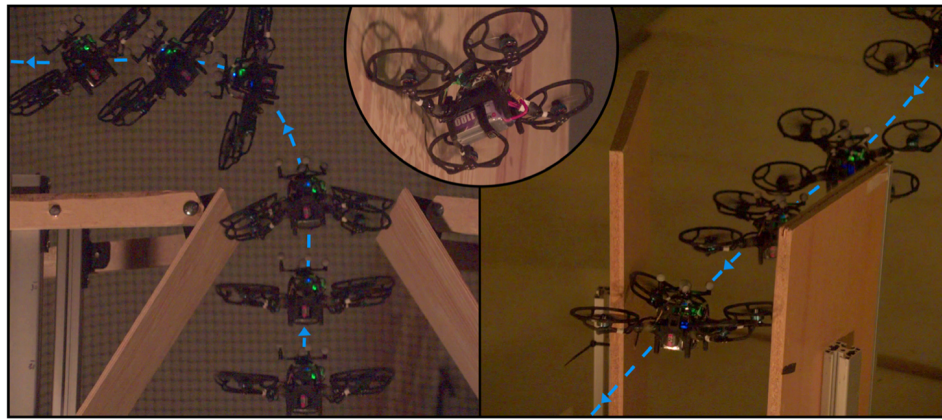


Figure 1. Morphy, the proposed compliant and morphologically aware flying system, demonstrating its effectiveness and robustness while squeezing through a vertical (left) and horizontal (right) passage, both smaller than the nominal dimension of the system, as well as handling a collision with a rigid obstacle at 3 m s^{-1} (middle).

allocation that considers the real-time feed from the Hall-effect sensors and thus the dynamic pose configuration of each motor and propeller. We also use this information to investigate the stationary and time-varying properties of the joints, as well as investigating their impact on the dynamics of the closed-loop system. The latter study is used to inform the design of a notch filter for mitigating the effects of the joint-induced dynamics from the tracking performance of Morphy. To the authors' best knowledge, this is the first work presenting the integration and utilization of 3D Hall-effect sensors for feedback measurements on a quadrotor design. This design choice allows Morphy to sense its current morphology, account for it during control allocation, and efficiently recover from collisions, thus further distinguishing it from previous designs.

The developed system's flying performance and overall capabilities are tested in a motion capture environment, both in free flight and collision scenarios. Initially, we report flight times for comparison between Morphy and an equivalent rigid design (referred to as Rigid Twin) under different circumstances, providing insights into how the introduced flexible joints negatively affect the system's endurance and how this effect can be mitigated through filtering. Then, we present the results of drop tests, conducted with collision speeds with the ground up to 7.6 m s^{-1} to evaluate the superior mechanical resilience of Morphy compared to its Rigid Twin. Subsequently, results of free flight circular trajectory tracking with the system flying at 1.5 m s^{-1} are reported. The closed-loop system's performance is then assessed on straight trajectories leading to collisions with speeds up to 3.0 m s^{-1} . Simultaneously, the system's ability to recover control post-collision is also demonstrated, showcasing its robustness resulting from the compliant design and effective control. Importantly, we further illustrate the robot's capability to navigate through openings more narrow than its own dimensions by passively morphing its shape exploiting its compliant design. This includes passing through narrow wedge-like structures both within horizontal and vertical flight.

The structure of this article is as follows. Section 2 presents relevant work in designs of soft flying robots. Section 3 outlines the design of the proposed robot, while Section 4 covers its

modeling and Section 5 details control. Experimental findings are then reported in Section 6, while conclusions are finally drawn in Section 7.

2. Related Work

The literature presents a niche set of studies that explicitly address how flexible and rigid components interact in quadrotors, and broadly multirotor systems, as well as how morphology awareness can be achieved onboard flying robots.

Within the realm of CT-MAVs, the closest subset of design realizations to the work presented in this manuscript are those involving elastic or compliant parts thus facilitating the incorporation of softness into their structure. As compared to the conventional completely rigid systems, these elastic designs can offer improved resilience and performance when the robot comes in contact with the environment by damping collision forces and lessening the impact effects. In refs. [9,10], the authors introduce a soft aerial robot inspired by the exoskeletons of arthropods. This robot combines a protective cage with the main frame into a semirigid design featuring soft joints. It weighs less than 250 g and has been shown to mechanically withstand collisions at speeds of up to 7 m s^{-1} . The researchers in ref. [11] present another type of aerial vehicle designed to withstand high-speed collisions and resume operations after impact relying on icosahedron tensegrity structures. When newly constructed, the proposed system is able to withstand a couple of drops from 7 m, corresponding to an impact speed of 11.7 m s^{-1} . The research described in ref. [12] introduces the initial version of resilient microflyer, a quadrotor equipped with a rigid protective frame along with compliant flaps. However, due to their structural geometry, none of the above mentioned designs allow these systems to fit through passages smaller than their nominal cross section. The study presented in ref. [8] on the other hand, introduces a quadrotor that incorporates a passive folding mechanism for its arms and protective shrouds, allowing not only to reduce collision risks but also facilitating the quadrotor to navigate through extremely narrow passages by passively adjusting

its geometry. Likewise, SquAshy^[13,14] represents a multimodal system designed for exploring confined spaces that also demonstrated squeeze-ability capabilities. Employing a different approach to softness, namely through soft and self-recovering propellers, the work in ref. [15] offers enhanced survivability in case of collisions but does not consider the potential benefits of overall airframe morphing and especially elasticity on the multirotor's arms. Utilizing a sensorized shell for contact sensing, the authors in ref. [16] enable a drone to push and slide past compliant obstacles, with unknown elastic properties, using an optimization-based controller that incorporates constraints for safety and an objective for damping interaction-induced oscillations, thus enabling collision-tolerant navigation through cluttered environments.

Research focusing on morphing and foldable MAVs has also yielded promising results beyond CT-MAVs.^[17] Even though most of these designs revolve around the integration of additional actuators responsible for morphing, like servos,^[18–20] linear actuators,^[21] or passive hinges,^[22] this type of design approach shows impressive results when it comes to navigating narrow gaps or generally adapts the system's geometry to fulfill a specific task. However, the majority of such systems relies on rigid mechanical components which in turn limits their ability to safely collide and broadly interact with surfaces or to adapt to their surroundings. In addition, the integration of further actuators typically increases the weight of the system, while several of the foldable designs do not simultaneously focus on collision tolerance.^[19]

On the contrary, focusing on advancing a robot's capability to adapt its body morphology and robustify its interaction with various environments, an intriguing approach for developing aerial robots involves leveraging materials-based strategies from soft robotics.^[23,24] These methodologies can pave the way to the creation of aerial robots equipped with soft robotic elements like soft structures, sensing, and actuation.

Investigating the possibility of constructing fully soft-bodied aerial robots, the authors in^[25] demonstrate the ability of a fully TPU 3D-printed unmanned aerial vehicle to perform full-body perching, specifically landing and stabilizing on pipelines and irregular surfaces without the need for an auxiliary system. As the researchers point out, strong nonlinear elastic dynamics appear as softness increases, which translates to complex modeling and difficult control. Following a slightly different approach, the authors in ref. [26] propose a novel reconfigurable quadrotor whose arms are based on soft pneumatic actuators, yet results are reported in simulation only. As opposed to fully soft airframe realizations, other researchers utilize a mixture of flexible, rigid, and soft materials with integrated mechanical shape-changing and sensing abilities. In the work of ref. [7], a quadrotor with a dual-stiffness frame that rigidly withstands aerodynamic loads within the flight envelope is presented, while the system can soften and fold during a collision to avoid damage. Finally, more specific to morphologically-aware flying robots, is the work of ref. [27], in which the authors define a compensation scheme to address the loss of thrust due to the overlap between the main body and the propellers.

3. System Design

This section overviews the airframe and flexible joint design of Morphy.

3.1. Airframe

Morphy is made by a combination of rigid and soft components and it is designed with the goals of being compact, lightweight, agile, compliant, and morphologically aware. In particular, the main central base and the motor housing are 3D printed with carbon fiber-reinforced polylactic acid (CF-PLA) which, compared to standard PLA, improves stiffness and strength while maintaining ease of manufacturing. The central base is connected to each motor housing via custom-designed flexible joints. These, as opposed to the stiff CF-PLA, are instead made of Elastic Resin 50A V2,^[28] 3D printed with a Formlabs 3L resin printer. Parts 3D printed with this type of material bend, stretch, compress, and hold up to repeated cycles without tearing and spring back to their original shape, fitting perfectly for our application. Each flexible joint is secured in between the rigid components with cured epoxy ARALDITE 2031-1.

The platform features four XING 1404, 3000 kV DC brushless motors, each equipped with a five-blade HQ Prop Duct-T75 mm propeller. It is powered by a 1100 mAh lithium polymers high-voltage (LiPoHV) battery, with the desired motor speeds controlled by a ModalAI VOXL Mini 4-in-1 electronic speed controller (ESC).

Morphy further integrates a ModalAI Voxl2 Mini serving both the purpose of low-level autopilot and that of a powerful onboard computer. This compact and lightweight all-in-one board, based on the Qualcomm QRB5165 processor, delivers robust performance with its 64-bit octa-core Kryo 585 CPU running at up to 2.84 GHz and fits perfectly in our simple, compact, and lightweight but computationally powerful design.

Finally, the proposed system offers sensing to facilitate autonomous navigation and path planning: a time of flight imaging sensor,^[29] a tracking imaging sensor (OV7251),^[30] and two InvenSense ICM-42 688-P^[31] inertial measurement units, one used by the flight controller (FC) for the system's in-flight stability and the other to serve visual-inertial odometry capabilities.

All components onboard Morphy are listed in detail in Table 1 with their corresponding weight, and a visualization of the location of the most relevant components can be seen in Figure 2a. The presented design can be fabricated entirely with off-the-shelf components and 3D-printed parts.

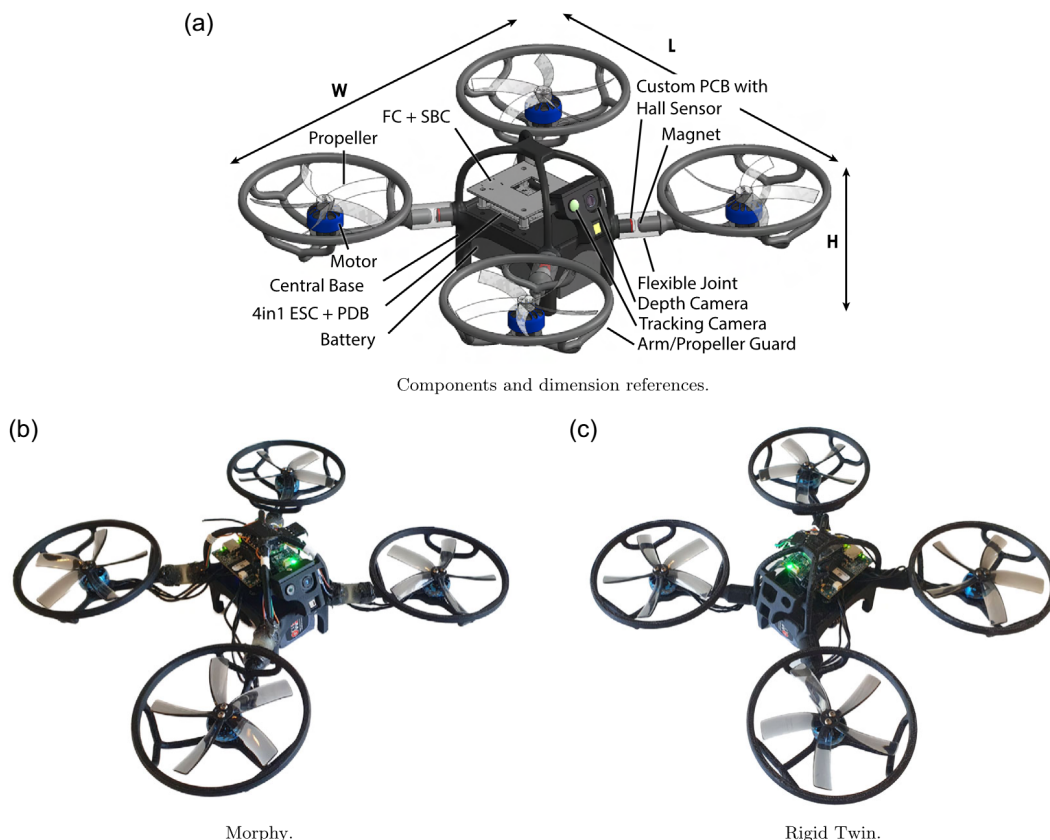
As mentioned in Section 1, during the development of Morphy, an otherwise equivalent rigid system, the Rigid Twin, of equal dimensions and mass was also built and utilized for comparison purposes against Morphy as a baseline. The main difference between the realized rigid system and the flexible one, apart from the flexible joint and the sensing solution related to it, is the sensing payload, which was not integrated in the rigid version to prevent unnecessary damage. Note from Table 1 that this mass is very low and thus negligible with respect to its role in the system dynamics. Both the final realization of Morphy and the Rigid Twin are depicted in Figure 2. The dimensions of Morphy are 23.9 × 25.2 × 7.9 cm (L × W × H) (when the arms are in their nominal configuration) with a total weight of 260 g. In this configuration, the system has a thrust-to-weight ratio of 3.3 and can hover for 12.5 min. Comparatively, Rigid Twin has a total flight time of 13.4 min. During all endurance tests, the battery is fully charged at takeoff and is at 20% capacity upon landing.

Table 1. Morphy components and corresponding weight distribution.

Component	Name	Weight [g]	
		Unit	Total
Motors	iFlight XING 1404 3000KV	9.5	38
Propellers	HQProp Duct-T75MMX5	3.5	14
	GNB 4 s 1100 mAh 60 C		
Battery	LiPoHV	–	90
Power distribution board and ESC	VOXL2 ESC Mini 4-in-1	–	12
Single-Board Computer and FC	VOXL2 Mini	–	–
Radio control receiver	iFlight ELRS	–	1.5
Arms and Propeller Guards	–	9	36
Flexible Joint	–	2.27	9.08
Central Base	–	–	30
Tracking Camera	–	–	0.46
Depth Camera	–	–	2.28
Custom PCBs + I2C Mux	–	–	6
Magnets	–	–	6
Miscellaneous	–	–	36.68
Total [Morphy]	–	–	260.0
Total [Rigid Twin]	–	–	252.2

3.2. Flexible Joint

To enhance the mechanical resilience of Morphy and investigate its performance both in free flight and in case of a collision event, we designed and prototyped a flexible joint and incorporated it between the central base plate and each arm supporting the motors. With the objective being to remain compact and lightweight but at the same time enabling the system with enhanced collision tolerance and body-shaping capabilities, the resulting joint takes the form of a cylinder measuring $14 \times 20 \text{ mm}$ ($D_J \times H_J$), with extrusions at the front and at the back to allow the insertion of the corresponding 3D-printed parts and sensing components. In particular, the flexible joint insertion on the side closer to the main frame allows the placement of a custom-designed printed circuit board (PCB) that integrates a TMAG5273 low-power linear 3D Hall-effect sensor,^[32] communicating with the onboard computer via I2C interface. This low-power component incorporates three separate Hall-effect sensors, each dedicated to measuring magnetic fields along the X, Y, and Z axes independently. On the other side of the flexible joint, closer to the motor and snap fitted inside the system's arm, a cylindrical neodymium magnet of size $4 \times 5 \text{ mm}$ is placed. The placement of these two components can be seen in **Figure 3**. This sensing solution is replicated on each arm and every sensor output is then fed to an Adafruit PCA9546


Figure 2. Illustrations showing a) the main components and reference dimensions of Morphy, b) a realization of the proposed system (Morphy), and c) its rigid equivalent (Rigid Twin). Note the lack of flexible joints and sensing cameras in the rigid counterpart.

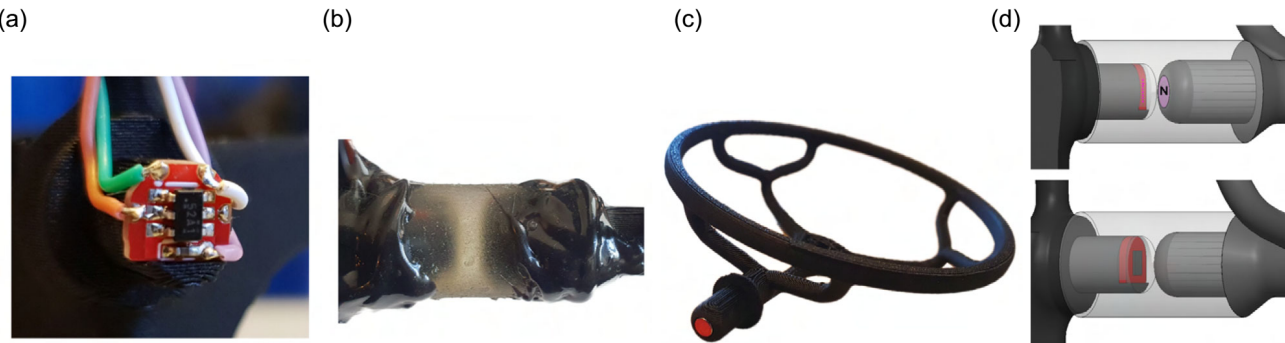


Figure 3. a) Custom PCB embedding the TMAG5273 3D Hall-effect sensor installed on the system before epoxy application, b) final flexible joint realization, c) details of neodymium magnet inserted in the arm, and d) computer-aided design of elastic resin flexible joint with both PCB and neodymium magnet, with marked north pole, inserted in the arm.

4-Channel I2C Multiplexer which is connected to the I2C bus of the VOXL2 Mini Linux machine. In this configuration, the magnetic field on the X, Y, and Z axes of all the four sensors is read in less than 2.5 ms and is thereby used for sensing the deflection in the elastic material of each joint, thus enabling shape awareness for the compliant Morphy design. In all the reported experiments of Section 6, the sampling frequency of the proposed solution is set to 300 Hz. Each additional flexible component contributes only 2.27 g to the overall mass as compared to the corresponding rigid arm design. A comprehensive analysis of the mechanical properties of the joint is provided in Section 4.3. This sensing solution, including the custom PCBs, the magnets, cabling, and the I2C multiplexer, does not add significant mechanical complexity to the system and contributes a total mass of only 21.08 g.

4. Modeling

This work makes use of different coordinate frames and the transformations between them. With respect to coordinate frames, these are the local world frame $\{W\}$, the central body

frame $\{B\}$, the four propeller disk frames $\{P_i\}$ (henceforth referred to as propeller for brevity), and Hall-effect sensor frames $\{H_i\}$. The propeller and sensor frames are indexed per arm i such that $i \in \{0, 1, 2, 3\}$, corresponding to the visualization in **Figure 4a**. Furthermore, let an arbitrary scalar, vector, and matrix be denoted as x , \mathbf{x} , and \mathbf{x} , respectively. Let the position of $\{A\}$ with respect to $\{B\}$ and expressed in $\{C\}$ be denoted $p_{BA}^C \in \mathbb{R}^3$. Let $\mathbf{R}_A^B \in SO(3)$ be the rotation from $\{A\}$ to $\{B\}$ and let q_A^B be the equivalent quaternion composed of the real scale η and imaginary vector ϵ .

4.1. Multibody Dynamics

The total quadrotor dynamics can be modeled as a multibody problem, with individual components obeying rigid-body dynamics (such as the set of parts of the robot's main body linked to the body frame $\{B\}$ and the arm–motor–propeller subsystem linked to the propeller frames $\{P_i\}$) and connected to one another by the elastic joints. As a result, the motion of each rigid body is a function of its own generated forces and torques (nonzero in the case of the propellers), external forces including gravity, as well as the

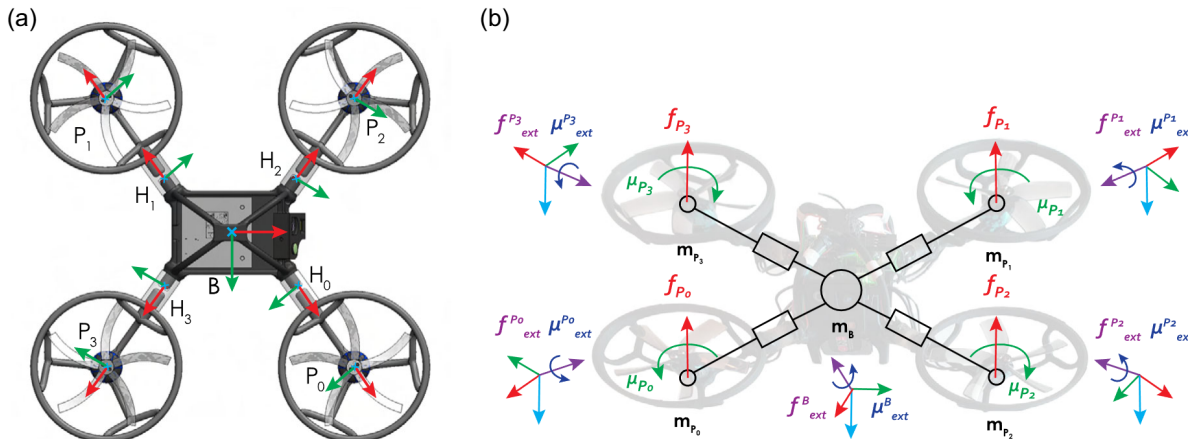


Figure 4. a) Reference frames utilized in this work, following the x-axis red, y-axis green, and z-axis blue convention. b) Illustration of forces and torques generated by each propeller frame, arbitrary forces, and torques generated by external sources and the elastic coupling to the body frame. Note that each of the depicted mass is affected by gravity and the external tridimensional forces and moments do not indicate a specific application point.

forces and torques generated in the other bodies comprising the robot and transferred through the elastic joints. A visualization of the force and torque generation from the propellers, as well as the interactions between rigid and elastic bodies, can be seen in Figure 4b. The mathematical relationships of these interactions will be discussed below. Note that in this work we consider that the propellers generate certain aerodynamic forces and moments based on their rotational speed and thus resort to the widely adopted simplification of the propeller disk, meaning we consider the aerodynamic effects as generated throughout a complete rotation. This allows us to consider the combination of each arm (without the soft joint), motor, and propeller as a single rigid part.

The physical properties of the rigid bodies are assumed known, such as the mass m as well as the inertia tensor J . Modeling starts with the robot's central rigid body $\{B\}$ which includes key elements such as the battery and electronics and has the simplest dynamics as it does not generate forces or torques itself. The dynamics are thus a function of the net forces and torques $\mathbf{f}_{\text{net}}^B, \boldsymbol{\mu}_{\text{net}}^B$ applied to the body frame, and the resulting angular velocity $\boldsymbol{\omega}^B$ and linear and angular accelerations $\mathbf{a}^B, \boldsymbol{\alpha}^B$, such that

$$\begin{bmatrix} \mathbf{f} \\ \boldsymbol{\mu} \end{bmatrix}_{\text{net}}^B = \begin{bmatrix} m_B \mathbf{I} & \mathbf{0} \\ \mathbf{0} & J_B \end{bmatrix} \begin{bmatrix} \mathbf{a} \\ \boldsymbol{\alpha} \end{bmatrix}^B + \begin{bmatrix} \mathbf{0} \\ \boldsymbol{\omega}^B \times J_B \boldsymbol{\omega}^B \end{bmatrix} \quad (1)$$

The net force and torque applied to the body frame can be expressed as the sum of forces and torques from sources external to the quadrotor $\mathbf{f}_{\text{ext}}^B, \boldsymbol{\mu}_{\text{ext}}^B$ and those generated by the propellers $\mathbf{f}_{P_i}, \boldsymbol{\mu}_{P_i}$. Actuation of a propeller generates force and torque that can propagate through the elastic joint, subject to the dynamics $g_{P_i}^B$ between $\{P_i\}$ and $\{B\}$, to the central body such that

$$\begin{bmatrix} \mathbf{f} \\ \boldsymbol{\mu} \end{bmatrix}_{\text{net}}^B = \begin{bmatrix} \mathbf{f} \\ \boldsymbol{\mu} \end{bmatrix}_{\text{ext}}^B + \sum_i g_{P_i}^B \left(\mathbf{R}_{P_i}^B \begin{bmatrix} \mathbf{f} \\ \boldsymbol{\mu} \end{bmatrix}_{P_i}^{P_i} \right) \quad (2)$$

where $\mathbf{f}_{P_i}^{P_i}, \boldsymbol{\mu}_{P_i}^{P_i}$ are the forces and torques generated by the propeller of $\{P_i\}$. The effects of the elastic joints on the overall system dynamics can already be seen here. The flexion of the joint causes rotation of the propeller frame, transforming the force and torques, and the dynamic characteristics of the joint causes a feedback loop through the forces and torques exchanged between different rigid bodies. The dynamics of any of the four arm units that involve the rigid structure, motor, and propeller, expressed in the associated $\{P_i\}$, can be similarly expressed as

$$\begin{bmatrix} \mathbf{f} \\ \boldsymbol{\mu} \end{bmatrix}_{\text{net}}^{P_i} = \begin{bmatrix} m_{P_i} \mathbf{I} & \mathbf{0} \\ \mathbf{0} & J_{P_i} \end{bmatrix} \begin{bmatrix} \mathbf{a} \\ \boldsymbol{\alpha} \end{bmatrix}^{P_i} + \begin{bmatrix} \mathbf{0} \\ \boldsymbol{\omega}^{P_i} \times J_{P_i} \boldsymbol{\omega}^{P_i} \end{bmatrix} \quad (3)$$

for the net force and torque $\mathbf{f}_{\text{net}}^{P_i}, \boldsymbol{\mu}_{\text{net}}^{P_i}$ applied to $\{P_i\}$. As mentioned, in this notation, the mass and inertia of a given arm expressed in the associated propeller disk is assumed to include contributions from the motor as well as the 3D-printed structures.

The net force and torque can be expressed as the sum of forces and torques from the propellers' own actuation, from sources external to the quadrotor, and from those resulting from other rigid-body elements (through the relevant elastic joint dynamics).

Those originating from other propellers first cause forces and torques in $\{B\}$, which can then propagate through the elastic joint connecting $\{P_i\}$ and $\{B\}$ such that

$$\begin{bmatrix} \mathbf{f} \\ \boldsymbol{\mu} \end{bmatrix}_{\text{net}}^{P_i} = \begin{bmatrix} \mathbf{f} \\ \boldsymbol{\mu} \end{bmatrix}_{\text{ext}}^{P_i} + \begin{bmatrix} \mathbf{f} \\ \boldsymbol{\mu} \end{bmatrix}_{P_i}^{P_i} + g_B^{P_i} \left(\mathbf{R}_B^{P_i} \begin{bmatrix} \mathbf{f} \\ \boldsymbol{\mu} \end{bmatrix}_{P_i}^B \right) \quad (4)$$

This closely resembles the rigid-body dynamics of a standard quadrotor with deviations resulting from the elastic joints: the subsequent potential for different motions between the body and propeller frames as well as the added dynamics of the elastic joint 2-mass coupling. Both of these effects will be further analyzed in Section 4.3.

4.2. Aerodynamic Forces and Moments

In the case of a quadrotor, its own forces and moments are generated by the four propellers mounted to the frame. A given propeller generates force along its z axis f_z and absolute moment about its z axis μ_z as a function of the propeller rpm u such that the norm takes the form

$$\begin{aligned} f_z &= k_\tau u^2 \\ \mu_z &= k_{\mu_z} u^2 \end{aligned} \quad (5)$$

where k_τ and k_{μ_z} are aerodynamic coefficients. The forces and moments from all propellers on the quadrotor expressed in the body frame are then a function of how the propellers are distributed spatially. Given the body frame position of a particular propeller P_i^B along with its relative orientation $\mathbf{R}_{P_i}^B$, the unit-length propeller thrust axis $\vec{\tau}_{P_i}^B$ is

$$\vec{\tau}_{P_i}^B = \mathbf{R}_{P_i}^B \begin{bmatrix} 0 \\ 0 \\ 1 \end{bmatrix} \quad (6)$$

such that the body frame force and moment for that propeller are

$$\begin{aligned} \mathbf{f}_{P_i}^B &= -k_{r,i} u_i^2 \vec{\tau}_{P_i}^B \\ \boldsymbol{\mu}_{P_i}^B &= \mathbf{p}_{B P_i}^B \times \mathbf{f}_{P_i}^B \pm_i k_{\mu_{z,i}} u_i^2 \vec{\tau}_{P_i}^B \end{aligned} \quad (7)$$

where \pm_i is negative for $i = \{0, 1\}$ and positive for $i = \{2, 3\}$ due to propellers rotating in opposite directions, as depicted in Figure 4b. Note that given the propeller–motor mounts and propeller guards are the same for each propeller in the proposed design, it is assumed that the aerodynamic coefficients are also the same. Therefore the i index on these coefficients will be dropped in the following sections.

4.3. Elastic Joint Modeling

Contrary to a typical quadrotor, the proposed design integrates elastic joints between the body and the propeller assemblies in order to better react to collisions and enable shape morphing capabilities. Therefore, the pose of any given motor is nonconstant during flight and especially under collision. More so, the elastic joints function as a dynamic coupling between rigid bodies. By design, the joint is incapable of significant compression or extension, meaning the experienced motion is primarily

in rotations. By design, azimuth and elevation rotations are those primarily experienced, as azimuth occurs naturally under collision and elevation occurs directly as a function of the force generated by the propellers. Torsional motion, while technically feasible, is thus negligible both due to joint construction and due to the nature of interactions experienced. These properties are modeled and analyzed in Sections 4.3.1 and 4.3.2.

In addition to the aforementioned transformations between coordinate frames which represent a model of the kinematics introduced by the soft joints, the elastic joints further contribute in affecting the dynamics. As an elastic component, it contributes energy-transforming and energy-dissipating effects, resulting in a system resembling a spring-damper connected to two masses. These properties are studied in Section 4.3.3 and 4.3.4, with data for investigating both the capacity for energy storage (like a spring) and for dissipation (like a damper).

4.3.1. Transformations

The deflection of an arm is modeled as a change in the spherical angle coordinates from the nominal resting position, as visualized in **Figure 5**. To distinguish between these two states, we introduce an additional coordinate frame for the nominal propeller position $\{\bar{P}_i\}$. The deflection from nominal for a given $\{P_i\}$ is defined as a function of the spherical angles of azimuth φ_i and elevation ϑ_i , which relate to the unit-length bearing vector \vec{b}_i of a point in space by

$$\vec{b}_i = \begin{bmatrix} \cos \varphi_i \cos \vartheta_i \\ \sin \varphi_i \cos \vartheta_i \\ \sin \vartheta_i \end{bmatrix} \quad (8)$$

Assuming the elastic joint functions kinematically as a revolute joint, that is, that the joint experiences insignificant shortening as it bends (achieved through construction), the

propeller position can be represented by a bearing vector and the known constant distance with respect to a local frame for each arm: the Hall-effect sensor $\{H_i\}$. This bearing vector can be reinterpreted as the rotation matrix corresponding to the quaternion which aligns the unit vector along x with the aforementioned bearing vector, $R(\varphi_i, \vartheta_i)$, neglecting torsion for the aforementioned reasons. Thus, the nominal propeller frame is defined as the state of the propeller when the angles are both equal to 0 and is related to the deflected position through the rotation by

$$p_{H_i P_i}^{H_i} = R(\varphi_i, \vartheta_i) p_{H_i \bar{P}_i}^{H_i} \quad (9)$$

As a result, the force and moment equations derived in Section 4.2 will change according to the effect of the deflections on a given propeller's position and positive thrust axis. The bearing vector is assumed to be measured from $\{H_i\}$ to the deflected propeller $\{P_i\}$ such that the position of the deflected propeller can be expressed as

$$p_{B P_i}^B = R_{H_i}^B R(\varphi_i, \vartheta_i) p_{H_i \bar{P}_i}^{H_i} + p_{B H_i}^B \quad (10)$$

The same modification can be done to update the propeller frame axis such that

$$\vec{r}_{P_i}^B = R_B^{H_i} R(\varphi_i, \vartheta_i) \begin{bmatrix} 0 \\ 0 \\ 1 \end{bmatrix} \quad (11)$$

The forces and torques generated in the body frame from each propeller, from Equation (7), can thus be rewritten using the new definitions for $p_{B P_i}^B$ and $\vec{r}_{P_i}^B$.

4.3.2. Calibration

The aforementioned spherical angles are measured with a 3D Hall-effect sensor–magnet pair embedded in the flexible joint,

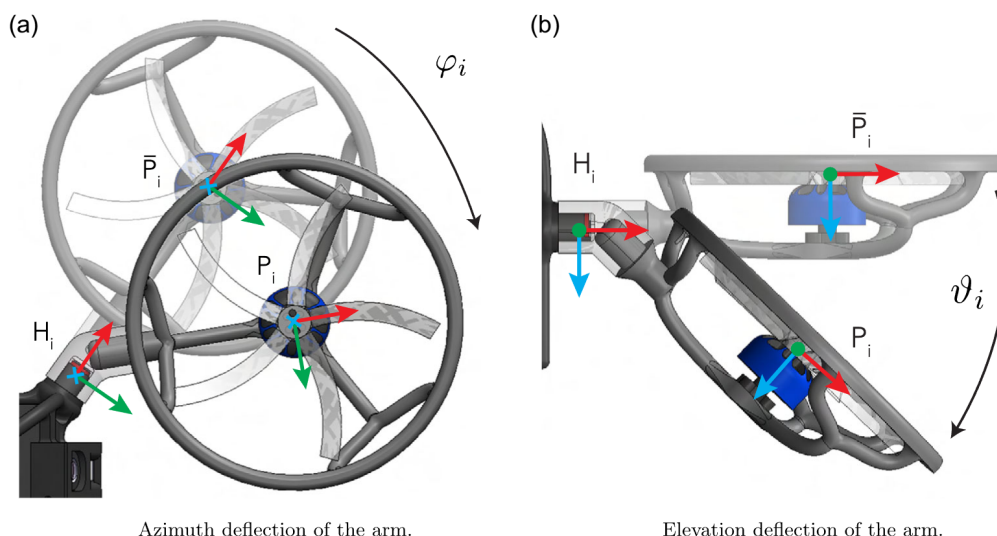


Figure 5. Visualizations depicting how the joint deflections are modeled and the physical relationships between the deflections and the measured angles.
a) Azimuth deflection of the arm. b) Elevation deflection of the arm.

as described in Section 3.2. Each of these sensors measures the 3D magnetic field corresponding to the magnet placed nearby. Since the permanent magnet is much stronger than the magnetic effects generated by the motors and other components on Morphy, the measurement of angle deflection can be considered isolated from such disturbances. However, due to physical constraints and difficulties associated with mounting as well as the fact that the elastic joint does not operate as a perfect revolute joint, the permanent magnet will not always be pointing directly at the sensor (as illustrated in Figure 5). Consequently, the magnetic field measurements cannot be directly construed as a bearing vector to the magnet. Instead, a linear model is employed to establish a relationship between the magnetic field measurements from the i th sensor $B_{i,x}$, $B_{i,y}$, $B_{i,z}$ and the azimuth and elevation angles, as per the

$$\begin{aligned}\varphi_i &= \alpha_{i,0} + \alpha_{i,x} B_{i,x} + \alpha_{i,z} B_{i,y} \\ \theta_i &= \beta_{i,0} + \beta_{i,x} B_{i,x} + \beta_{i,z} B_{i,z}\end{aligned}\quad (12)$$

where the coefficients are estimated using linear regression applied to motion capture data used to create the azimuth and elevation angle measurements. The result of this linear regression can be seen in **Figure 6** with the parameters shown in **Table 2**. Note that the figure visualizes the primary magnetic field along the x -axis, where primary is considered the axis with the largest parameter in Table 2. For example, azimuth measuring the magnetic field along the y -axis is the most significant indicator, followed by x , and with practically no information along the z -axis. This calibration was conducted per joint, and as shown in Table 2, the parameters present some variance per arm. This is attributed to the fact that each arm was—for prototyping reasons—assembled by hand, which is prone to some amount of misalignment and fabrication errors.

Table 2. Parameters found by linear regression, relating measured magnetic field to deflection along azimuth and elevation.

Angle	Arm	Coefficients				R^2	RMSE [deg]
		$\alpha_{i,0}$	$\alpha_{i,x}$	$\alpha_{i,y}$	$\alpha_{i,z}$		
Azimuth [φ_i]	$i = 0$	0.011	0.011	0.109	0	0.9694	2.0390
	$i = 1$	0.145	-0.001	0.095	0	0.9622	2.4900
	$i = 2$	0.021	-0.008	0.140	0	0.9524	2.6528
	$i = 3$	0.642	-0.010	0.129	0	0.9112	3.8786
		$\beta_{i,0}$	$\beta_{i,x}$	$\beta_{i,y}$	$\beta_{i,z}$		
Elevation [θ_i]	$i = 0$	0.214	-0.029	0	0.111	0.9724	1.8535
	$i = 1$	0.271	-0.022	0	0.090	0.9816	1.7239
	$i = 2$	0.108	-0.025	0	0.124	0.9525	3.0265
	$i = 3$	0.157	-0.024	0	0.115	0.8970	3.5808

4.3.3. Spring Characterization

To characterize the behavior of the flexible joints, we first analyze the deflection of individual arms under varying static loads. As described in Section 3, the joints are fabricated with Elastic Resin 50 A V2 using 3D printing techniques, resulting in components with hard-to-predict mechanical properties (such as Young's modulus and viscoelastic damping behavior). To determine the relationship between force and angular deflection of the joints, external forces are applied by attaching weights for both azimuth and elevation deflections. In order to do so, we construct a plumb line mechanism, with a hanging basket, attached to the center of the motor mount, which is then iteratively loaded with objects of known mass. After loading additional objects, we let

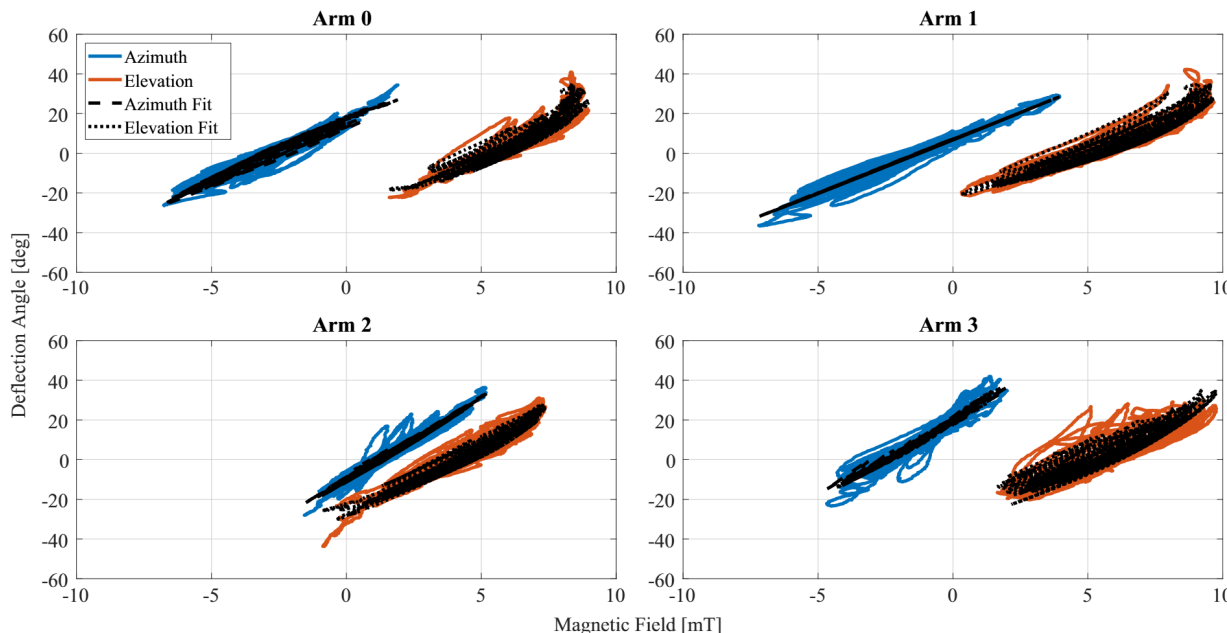


Figure 6. Visualization depicting the results of applying linear regression to the motion capture data in order to determine model parameters for calculating joint angles from magnetic field measurements.

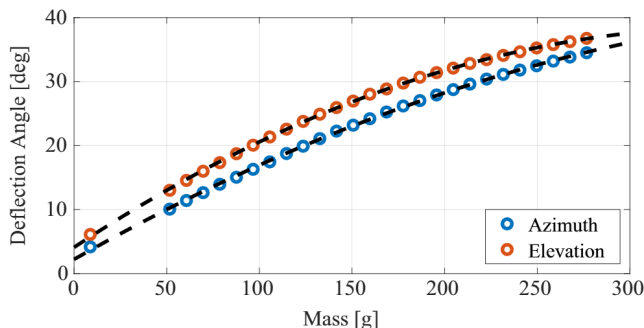


Figure 7. Angle displacement for both azimuth and elevation in relation to the attached weight. The dashed line represents the second-order polynomial fit.

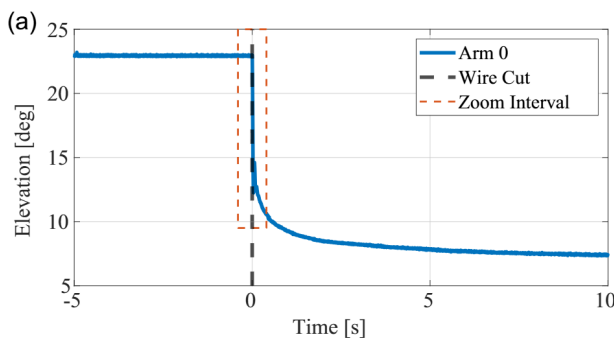
the oscillations stabilize, as adding weight perturbs the stability of the readings. The angle deflections are recorded versus the hung mass, and as shown in **Figure 7**, a second-order polynomial fits well to the collected data, indicating a quadratic response of the designed joint. The second-order polynomial in question can be written as a function of the force exerted by the hung mass m_h

$$\begin{aligned} \varphi_0 &= \gamma_0 + \gamma_1 m_h + \gamma_2 m_h^2 \\ \theta_0 &= \delta_0 + \delta_1 m_h + \delta_2 m_h^2 \end{aligned} \quad (13)$$

where γ and δ are the regression parameters, shown in **Table 3**.

Table 3. Joint polynomial parameters and linear regression statistics for arm 0.

Name	Coefficient	SSE	R ²	RMSE
Azimuth [φ_0]	γ_0	2.22	–	–
	γ_1	0.1643	0.7576	0.9996
	γ_2	-0.00017	–	–
Elevation [θ_0]	δ_0	4.094	–	–
	δ_1	0.1914	0.3947	0.9998
	δ_2	-0.00027	–	–



4.3.4. Dynamics

To further explore the behavior of the developed flexible joint under varying loads and disturbances, we setup a similar configuration as described in Section 4.3.3. This time, the goal was to investigate the joint dynamics and how the deflection angle evolves as a function of time. Like before, we hang a known mass from $\{P_0\}$, rigidly attached to a stable plane and without the ability to move, and cut the wire sustaining it once the system is at rest. During this process, we record the evolution of the measured angle over time as the mass hangs and subsequently drops. This setup allows us to record and analyze the joint's step response to the sudden load release, functioning as a step input, which provides valuable insights into its transient characteristics. The full time evolution can be seen in **Figure 8a** and with a shorter time horizon in **Figure 8b**, revealing the high-frequency oscillations. This experiment was conducted specifically along the elevation degree of freedom, but given the joints symmetric design similar behavior is expected in azimuth.

The elasticity of the designed joint and the corresponding dynamics that this introduces also impact the overall system's flight behavior. This characteristic can be seen in the step response presented here in **Figure 8**. As the joint is elastic, with a nontrivial structure, the modeling of this behavior goes beyond a simple linear mass-spring-damper system. Numerical analysis of the entire system, including elastic joint effects, is conducted in Section 5.2, demonstrating the impact of the added dynamics on flight behavior and possible mitigation of certain undesired side effects.

5. Control

The trajectory-tracking controller that used onboard the flying robot for this manuscript is a series of cascaded proportional integral derivative (P-PID) controllers for the position-linear velocity and attitude-angular rate systems, using the implementation from refs. [33,34], which are visualized in **Figure 9** (the control laws for which are described in Appendix A). The inputs of the controllers are setpoints for position, velocity, linear acceleration, and yaw while final outputs of the controller are the desired moments μ_{ref}^B and desired vertical thrust $f_{z,ref}^B$ which are transformed into actuator commands by the motor allocation

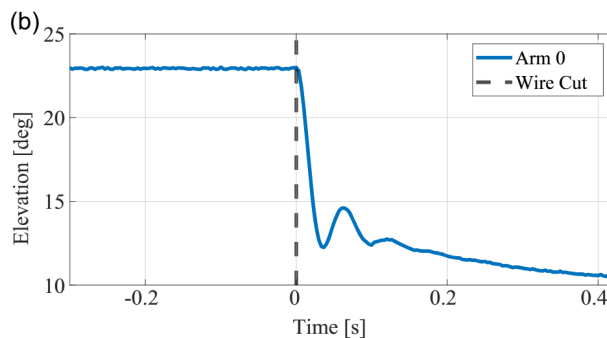


Figure 8. Figures depicting the time evolution of the elastic joint's elevation angle response to a step input realized by instantaneously removing the hanging weight. a) The full step response and b) Reduced time window to expose oscillations occurring just after the cut time. Note that due to the symmetric design of the elastic joint, a similar response is expected for the azimuth angle.

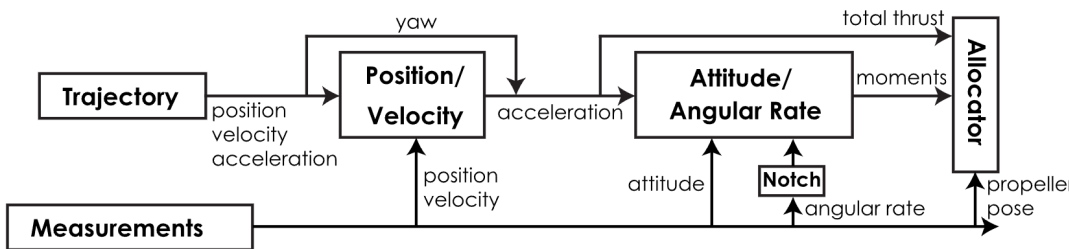


Figure 9. Block diagram showing signal flow in control architecture, including the proposed adaptive control allocation acting on measurements of propeller frame pose.

module. As the arms of Morphy experience flexion due to the elastic joints, a custom control allocation scheme is implemented.

5.1. Adaptive Allocation

Given desired forces and moments from the controller, the corresponding actuator commands are found through the actuator effectiveness relationship, simplified for quadrotors to ignore thrust along x and y .

$$\begin{bmatrix} \mu^B \\ f_z^B \end{bmatrix} = \mathbf{G} u^{\circ 2} \quad (14)$$

where \mathbf{G} is the actuator effectiveness matrix and u is the stacked vector containing actuator commands with the element-wise square operator $(\cdot)^{\circ 2}$. For quadrotors, this is a linear system of equations such that the actuator command u_{ref} can be found by the pseudoinverse $(\cdot)^{\dagger}$ as

$$u_{\text{ref}}^{\circ 2} = \mathbf{G}^{\dagger} \begin{bmatrix} \mu^B \\ f_z^B \end{bmatrix}_{\text{ref}} \quad (15)$$

Calculating the actuator effectiveness matrix for a standard quadrotor utilizes the modeling from Section 4.2. However, for Morphy, we instead use the updated equations from Section 4.3, taking into consideration the nonrigid joints and the measurements of their deflections and the impacted force and torques $\mu_{P_i}^B, f_{P_i, z}^B$. Then the revised morphology-aware actuator effectiveness matrix is calculated as

$$\mathbf{G}_i = \begin{bmatrix} \mu_{P_i}^B \\ f_{P_i, z}^B \end{bmatrix} \forall i \in \{0, 1, \dots, 3\} \quad (16)$$

where \mathbf{G}_i is the i th column of \mathbf{G} . This is a key modification to the conventional control allocation of rigid quadrotors and its importance is amplified when the robot's arms experience significant deflections in azimuth φ_i or elevation θ_i .

5.2. Frequency Response of the Robot's Main Frame Motion Dynamics

To understand how the integrated flexible joints and, effectively, the moving arms onboard the system affect the system in free flight, we command the system to follow a chirp signal, isolated

in a specific axis, to capture the spectrum of frequencies. The trajectory's setpoints are defined as

$$\begin{aligned} x(t) &= A \cos(\omega(t)t) \\ y(t) &= B \cos(\omega(t)t) \\ z(t) &= C \cos(\omega(t)t) \\ \omega(t) &= \omega_0 + \frac{(\omega_f - \omega_0)}{T} t \end{aligned} \quad (17)$$

where the scalars A , B , and C are set to nonzero when the specific direction of motion is considered and ω linearly increases from $\omega_0 = 1 \text{ rad s}^{-1}$ to $\omega_f = 2.5 \text{ rad s}^{-1}$ during the duration T of each experiment. The total duration of each run is set to 60 s.

We run the chirp signal for x , y , and z separately, setting the scalars $A = B = 1.2$ and $C = 1.0$, respectively. These values were chosen such that the drone utilizes as much space as possible within the utilized test area when flying this trajectory, offering more time to reach higher velocities. As such, a different value is used for C due to spatial constraints imposed by the employed motion capture arena.

This experiment highlights the frequency-domain effects of the elastic joints and allows to guide how these are handled such that performance is not degraded. First, the chirp is run on the Rigid Twin as well as Morphy, the results from which are shown in the first two rows of **Figure 10**. Comparing the Rigid Twin and Morphy, one can see the impact of the elastic joints in this peak at $\approx 23 \text{ Hz}$ in the fast Fourier transform (FFT) of the angular rate measurement (see **Figure 10a**). As this is an undesirable high-order effect, a notch filter is applied to the angular rate measurements such as to reduce the impact. In practice, it was determined that a notch filter with center at 28 Hz and bandwidth 20 Hz mitigated the impact best. The result of repeating the chirp experiments with Morphy, with the notch filter active, can be seen in the final row of **Figure 10**, demonstrating significant reduction of this peak in the frequency response of the robot dynamics.

Note that a similar effect can also be seen in the controller torque setpoints, in **Figure 10b**. Given that the torque setpoint is calculated by the controller as a function of the angular rate measurement, it is expected that here a similar peak at $\approx 23 \text{ Hz}$ can be seen. Like before, this effect is significantly reduced by the addition of the notch filter. The benefits of doing so are twofold: first, reduction of the oscillations in the measurements and actuation benefits the tracking performance, while it also has a significant impact on the flight time, which is discussed in Section 6.1.

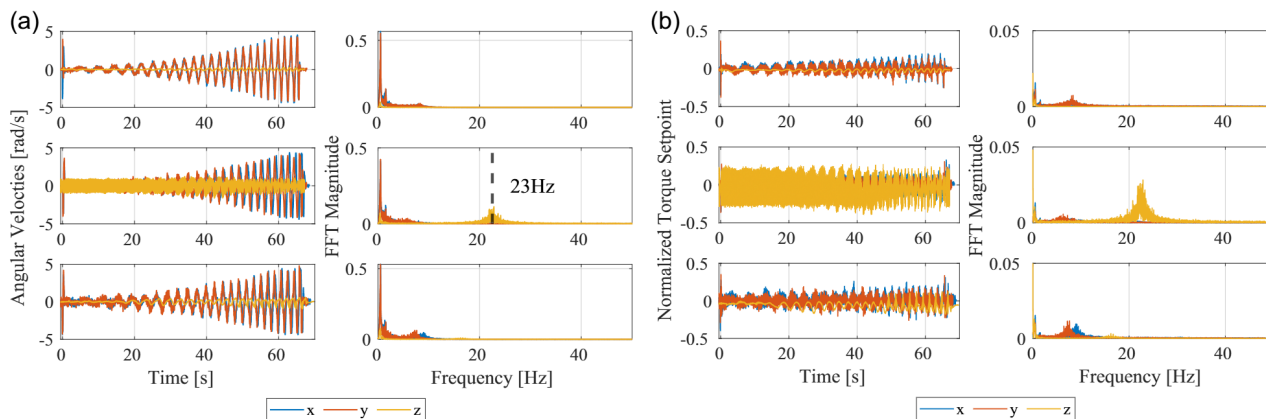


Figure 10. a) Angular rate measurements registered onboard Morphy during the execution of the chirp signal in the x, y, and z directions and corresponding FFT response. b) Torque setpoints registered onboard Morphy during the execution of the chirp signal in the x, y, and z directions and corresponding FFT response. The first row corresponds to the Rigid Twin, the second to Morphy without the angular rate notch filter enabled, the third to Morphy with the angular rate notch filter enabled. In each tile, each x, y, and z plotted signals are extracted from the corresponding flight in which the specific direction of motion is considered. Note that both the angular rate measurements and the torque setpoints are logged at 275 Hz.

6. Experimental Evaluation

In this section, we present the experimental evaluation of the proposed design across six distinct scenarios. First, we present a comparison of the respective flight times of the Rigid Twin of Morphy against Morphy using the developed adaptive control allocation along with the controller described in Section 5. Note that the feedback controller was tuned on the Rigid Twin. Second, we conduct drop tests for both the proposed system and the Rigid Twin to empirically validate the maximum permissible collision speed of the developed system and study in-collision deformations using a Kron Technologies Chronos 1.4 high-speed camera, recording the event at 1069 frames per second. Third, we evaluate the proposed adaptive allocation scheme against the nominal one on Morphy while tracking a circular trajectory and compare both to the Rigid Twin equivalent system. Fourth, we perform in-flight crash tests at speeds up to 3 m s^{-1} to evaluate the system's performance in collision with a fixed obstacle, the significant deflection of the arms, and the robot's recovery capabilities. Finally, we conduct two distinct experiments to evaluate the squeeze-ability and shape-morphing capabilities of Morphy in both the horizontal and the vertical plane. For the tracking and collision experiments shown below, we show position and velocity estimates (logged at 10 Hz) obtained by fusing motion capture positioning onboard the quadrotor in addition to the measured deflection angles (logged at 100 Hz) sourced from the custom sensing solution outlined in Section 3. Note that, unless mentioned, every experiment involving Morphy makes use of the notch filter described in Section 5.2. Without this addition, the induced dynamics of the joints impose undesired effects to the closed-loop behavior, including over-actuation resulting in oscillations during stable flight.

6.1. Flight Time

For this evaluation, we conduct endurance tests and compare the respective flight time of the Rigid Twin against Morphy using

our developed adaptive control allocation along with the controller described in Section 5, which is tuned on the Rigid Twin. Flexing in the arms demonstrates to have negative effects on the control tracking performance and the system's flight time. The system is experiencing oscillations due to the introduced flexible components which are amplified, or at least retained, by the controller, alongside significant nonzero dynamics with higher time constant. As a result, significant improvements in both the control performance and flight time are achieved with the addition of the notch filter specifically designed for these newfound dynamics. The effects of these insights on the chirp test and flights times can be seen both with and without the notch filter in Section 5.2 and **Table 4**. As described in Section 3, during all endurance tests, the battery is fully charged at takeoff and is at 20% capacity upon landing.

6.2. Drop Test

To assess the effectiveness of the proposed system design in managing collisions, we first start performing a series of drop tests. These experiments involve dropping the frame, equipped with a mass representing the final design, from predetermined heights. The deflections of the joints are then evaluated and the maximum speed that could be reached before causing damage to the system is determined. All successful drop heights can be seen in **Figure 11**, where the maximum attempt height with Morphy was 2.9 m resulting in a collision with the ground at $\approx 7.6 \text{ m s}^{-1}$. We then repeat the same experiment using the Rigid Twin of

Table 4. Flight time comparison: rigid twin, Morphy with angular rate notch filter disabled, Morphy with angular rate notch filter enabled.

Frame type	Flight time [min:s]	
Morphy	Rigid Twin	13:20
	w/out Notch	9:00
	w/ Notch	12:30

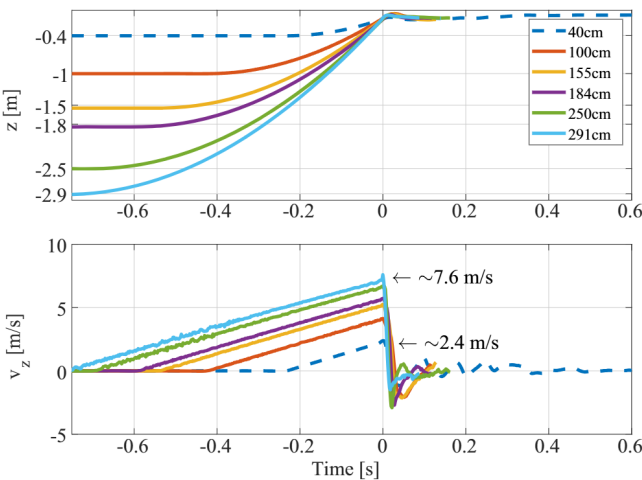


Figure 11. Motion capture results of the drop tests, displaying the evolution of height (z) during the falls, as well as the vertical velocity based on numerical differentiation. The flexible frame can be seen sustaining crashes at much higher speeds than the Rigid Twin, with final successful crashes of $\approx 7.6 \text{ m s}^{-1}$ (flexible) versus $\approx 2.4 \text{ m s}^{-1}$ (rigid).

Morphy, loaded with an equivalent mass. This rigid counterpart successfully survives a drop from 0.4 m, resulting in an impact speed of $\approx 2.4 \text{ m s}^{-1}$, as shown in Figure 11. However, gradually increasing the drop height to 0.61 m, corresponding to an impact speed of $\approx 3.1 \text{ m s}^{-1}$, results in a fatal crash for the Rigid Twin.

This demonstrates the significantly better crash resilience of the elastic design in comparison to its rigid counterpart. Additionally, **Figure 12** clearly shows the extreme deflections of the arms, underlining the essential role of the designed flexible joints to allow the system to sustain high-speed collisions.

6.3. Trajectory Tracking in Free Flight

To test the performance of the proposed system during free flight, we command it to follow a fixed circular trajectory. The trajectory's setpoints are defined using the parametric equations for a circle.

$$\begin{aligned} x(t) &= a \cos(\omega t) \\ y(t) &= b \sin(\omega t) \\ z(t) &= c \end{aligned} \quad (18)$$

where a and b are scaling parameters, ω is the angular speed, and c is the chosen flying height. To improve tracking performance, the first and second derivatives of these position signals are analytically computed and input to the controller as feedforward terms following Section 5. The controller's ability to track such a trajectory for both the nominal and adaptive control allocation variants, alongside the performance of the baseline Rigid Twin of same weight and size with the nominal controller, specifically built for this purpose, is demonstrated in **Figure 13** on a trajectory with $a = b = 1.2 \text{ m}$, $c = 1.8 \text{ m}$, and $\omega = 1.5 \text{ rad s}^{-1}$. It is noted that in free flight and for small accelerations the system

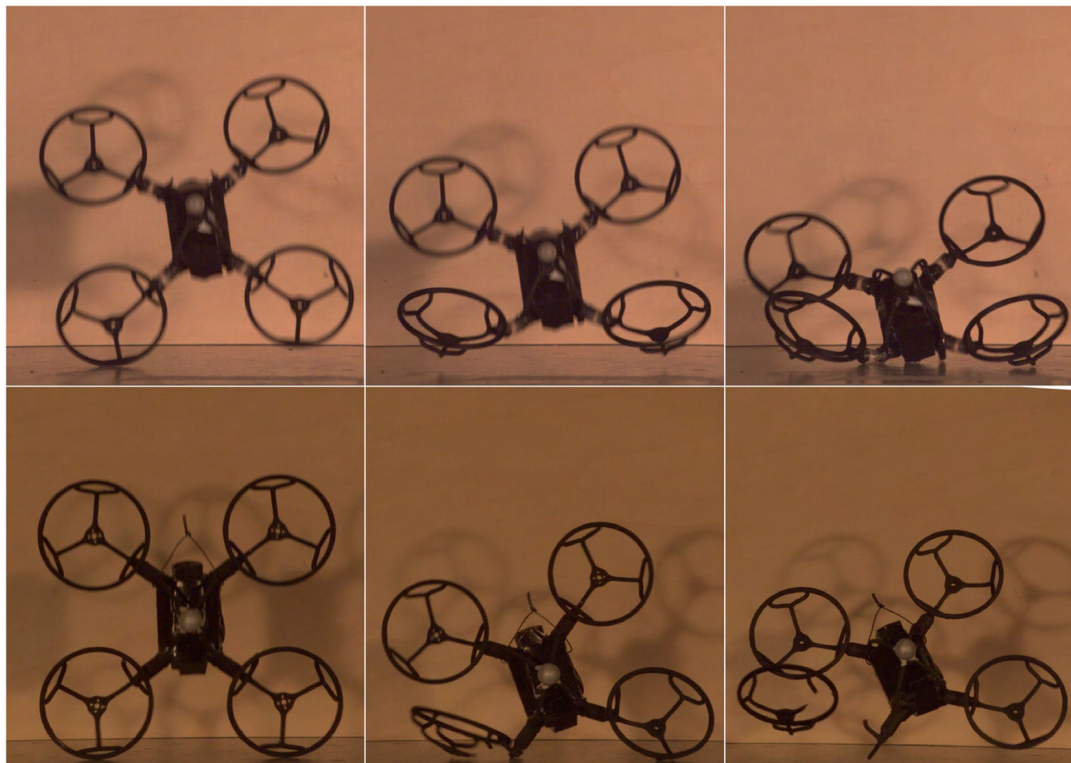


Figure 12. Comparison: the top row shows the proposed design of Morphy with integrated flexible joints, surviving a drop from 250 cm. The bottom row depicts the Rigid Twin of the system breaking during a drop from 60 cm. Both frames are loaded with a dummy weight to match the real system's mass at impact with ground.

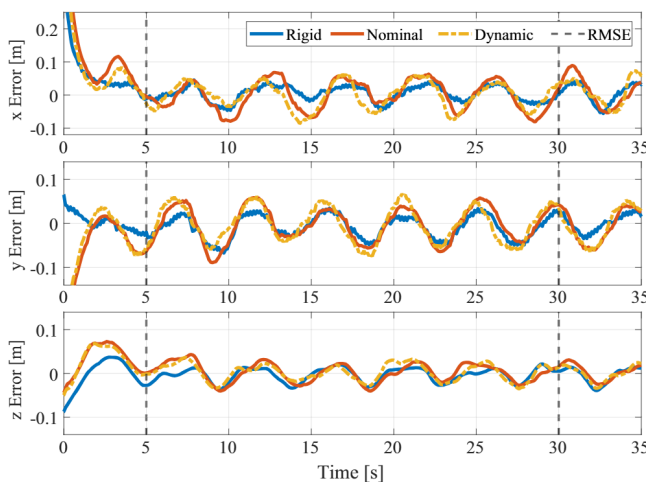


Figure 13. Error in tracking the circular trajectory references as per Equation (18), where a and b are set equal to 1.2 m, at a speed of 1.5 m s^{-1} , at an altitude of 1.8 m above the ground for the Rigid Twin (with the nominal controller, marked in blue), and Morphy using either the nominal (red) or the adaptive control allocation method (yellow dash). The black dashed lines mark the time interval used for the root mean square error (RMSE) calculation. The time selection guarantees that the system is already on track in the commanded trajectory and not in a takeoff or landing phase.

experiences minimal arm deflections; thus, both the nominal and adaptive control allocation methods result in a similar tracking error, still with slight improvement of the adaptive control allocation over the nominal one, and both performed worse than the Rigid Twin, as reported in **Table 5**.

6.4. Midflight Collision and Recovery

In this set of experiments, we evaluate the proposed design's ability to withstand midflight collisions and subsequently return to stable hover. For this purpose, we instruct Morphy to follow a straight-line trajectory in the xy -plane at a fixed altitude. A rigid obstacle is placed at a known distance from the starting position of the trajectory. Then, a final recovery setpoint is added, commanding the quadrotor to hold a position 0.4 m away from the obstacle. These adjustments aim to encourage the robot to stabilize its attitude and position postcollision, guaranteeing consistency across iterations of the experiment. An instance of Morphy

Table 5. Trajectory tracking RMSE for the different configurations of Figure 13, calculated after trajectory tracking seems to converge (from time 5–30 s). The time selection guarantees that the system is already on track in the commanded trajectory and not in a takeoff or landing phase.

Type	RMSE [m]		
	x	y	z
Rigid	0.0230	0.0273	0.0159
Nominal	0.0433	0.0384	0.0211
Adaptive	0.0383	0.0388	0.0189

colliding with the obstacle at 3 m s^{-1} can be seen in **Figure 14a**. In **Figure 14b**, the measured azimuth and elevation angles of the front left and front right arms are depicted, alongside the robot's position along the world frame y axis and the associated velocity. As shown, the increase of the impact speed leads to a greater arm deflection. Furthermore, the same figure displays time-based plots of key robot states, including the y velocity response, offering deeper insights into the system's resilient collision reaction and subsequent recovery to a stable hover.

At greater speeds the momentum is such that the deflection of the arms alone does not dissipate enough force to prevent the body of the quad rotor from impacting. This is the case for both of the 2 and 3 m s^{-1} trajectories shown in **Figure 14**. Even then, the elastic joints manage to dissipate sufficient force and, although the rigid frame suffers impact, Morphy survives the collision. Note that, in comparison, similar impact speeds are entirely unsurvivable by the Rigid Twin, as shown in Section 6.2.

6.5. Horizontal Squeeze

A key motivation for the design of Morphy is to facilitate the ability to morph passively and explore the benefits this offers in navigation skills. In this experiment, we showcase how the proposed design can effectively utilize its squeeze-ability properties to navigate through openings more narrow than its nominal dimensions. Specifically, Morphy is commanded to follow a straight-line trajectory in the xy -plane at a fixed altitude while encountering an obstacle placed in its path. The obstacle is shaped like a wedge with wide entry and narrow exit points. Selected frames from the Chronos high-speed camera footage of this experiment, where the robot is compressed to 22 cm in width, are illustrated in **Figure 15**, while corresponding time response graphs and registered angle deflections are provided in **Figure 16**. Note that the nominal width of the robot, W , is equal to 25.2 cm, as described in Section 3.

6.5.1. Minimum Speed

As Morphy passes through the wedge primarily by virtue of its momentum and ability to deflect its arms, it is interesting to study how this ability changes in relation to the commanded speed. To that end, a series of experiments are conducted at different speeds which demonstrate successful passage traversal with commanded forward speeds as low as 0.15 m s^{-1} (depicted in **Figure 17**). However, it was found that the platform's behavior during the collision event changes as a function of speed. Low-speed trajectories (e.g., 0.15 m s^{-1}) result in the velocity of Morphy going to zero as it does not enter with sufficient momentum to pass through uninterrupted. In order to keep following the commanded trajectory, the system is forced to increase its motor commands until the static friction is overcome and the wedge is eventually traversed. Subsequently, commanding the system to traverse the wedge obstacle with a forward speed of 1 m s^{-1} allows Morphy to pass more seamlessly. Note that even slightly asymmetric approaches cause changes in attitude which generally enable Morphy to pass through without necessarily deflecting all arms. Finally, higher speeds result in wedge interaction times

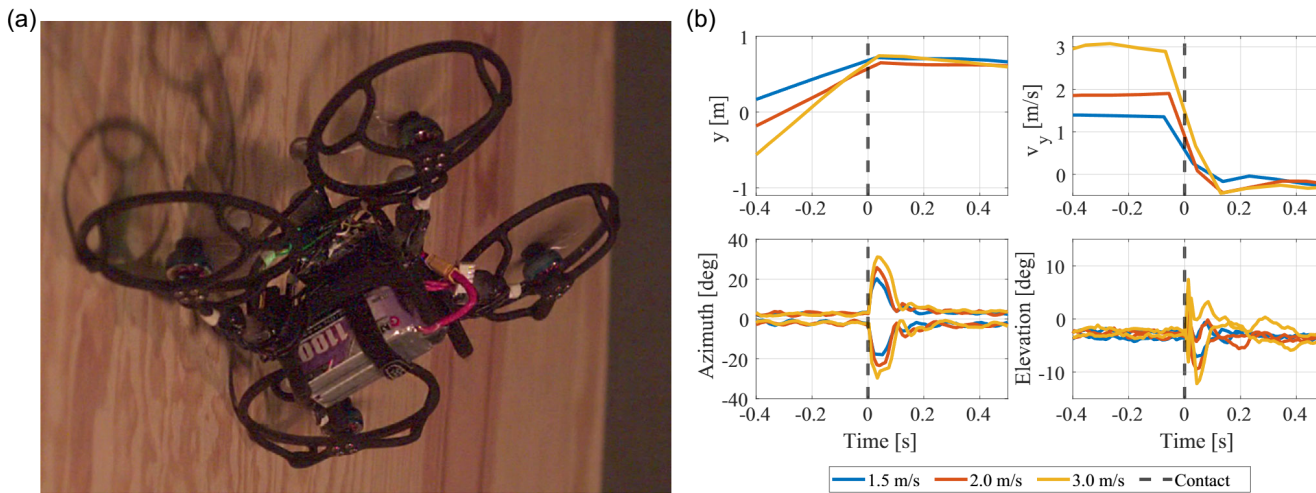


Figure 14. a) Extracted video frame of Morphy colliding at 3 m s^{-1} . b) y position, v_y velocity, and registered angle deflections of both azimuth and elevation of the front-left (negative deflection) and right (positive deflection) arms as the system flies toward collision. Note the increase in the deflection as the impact speed increases. In the velocity plot, the apparent speed reduction before the collision point is a plotting artifact derived from the low sampling rate, as discussed at the beginning of Section 6.

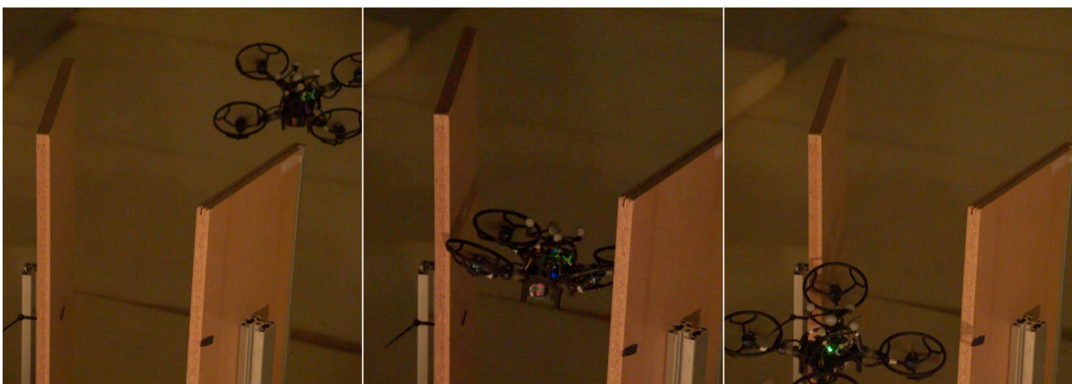


Figure 15. Indicative frames captured by the Chronos high-speed camera during the horizontal squeeze experiment.

too short for significant attitude change, as such arms are forced to deflect, letting Morphy to squeeze through.

6.6. Vertical Squeeze

In a manner analogous to the horizontal squeeze experiment, in this test we showcase how the proposed design can effectively utilize its squeeze-ability properties to navigate vertical openings more narrow than its nominal cross section. In this final experiment Morphy is commanded to follow a straight line trajectory in the yz -plane while an obstacle is placed in its path. The obstacle is shaped like a wedge with wide entry and narrow exit points. A collage depicting the motion and morph shaping capabilities of the system, where the robot compressed to 22.5 cm, can be seen in Figure 18 using frames from the Chronos high-speed camera. Corresponding time response graphs and angle deflections registered by each arm in contact with the wedge are provided in Figure 19. Note that the nominal width of the robot, W , is equal to 25.2 cm, as described in Section 3.

The proposed system is able to repetitively collide, squeeze both horizontally and vertically, and survive all of the above described scenarios without any damage. It is highlighted that in all of the experiments not a single propeller has to be changed. Likewise, no structural damage to the airframe was registered. This points out that incorporating soft components into the framework of multirotor airframes introduces a previously unexplored level of adaptability, enabling navigation through demanding environments with enhanced resilience, sustaining high-speed collisions with their surroundings, facilitating shape-morphing, and maneuvering through passages narrower than their nominal dimension.

6.6.1. Impact of Arms Bending

To further evaluate the impact of the elastic joints on the flying behavior of Morphy, the 3 m s^{-1} experiment from Section 6.6 and Figure 19 is analyzed. Following the derivation in Equation (11), and following the reference frames notation

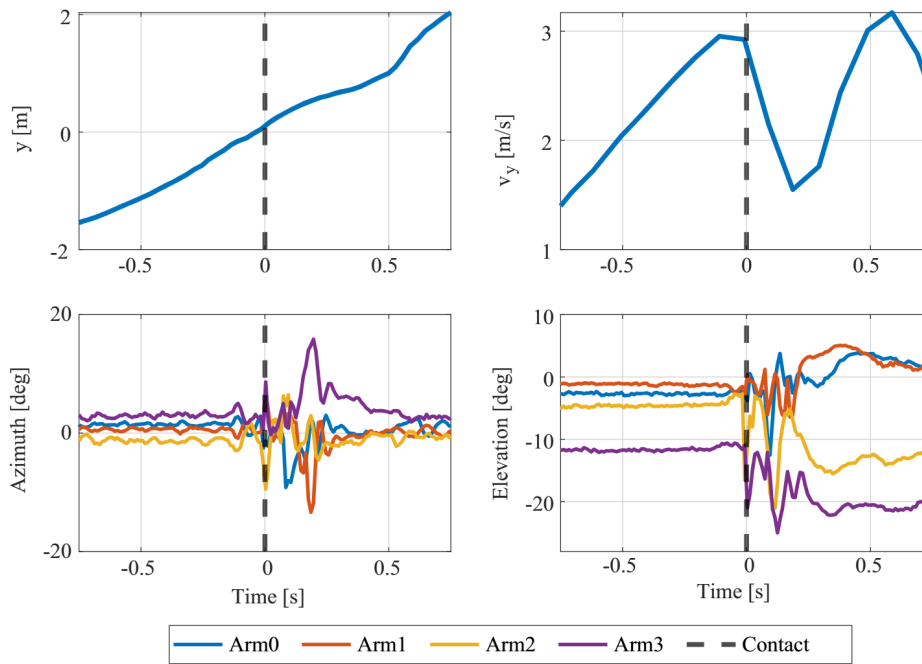


Figure 16. Time series and onboard recorded angle deflections of the horizontal squeeze experiment with the first contact point marked. Position on the y axis, associated velocity, as well as the azimuth and elevation angles of the four soft arms are depicted.

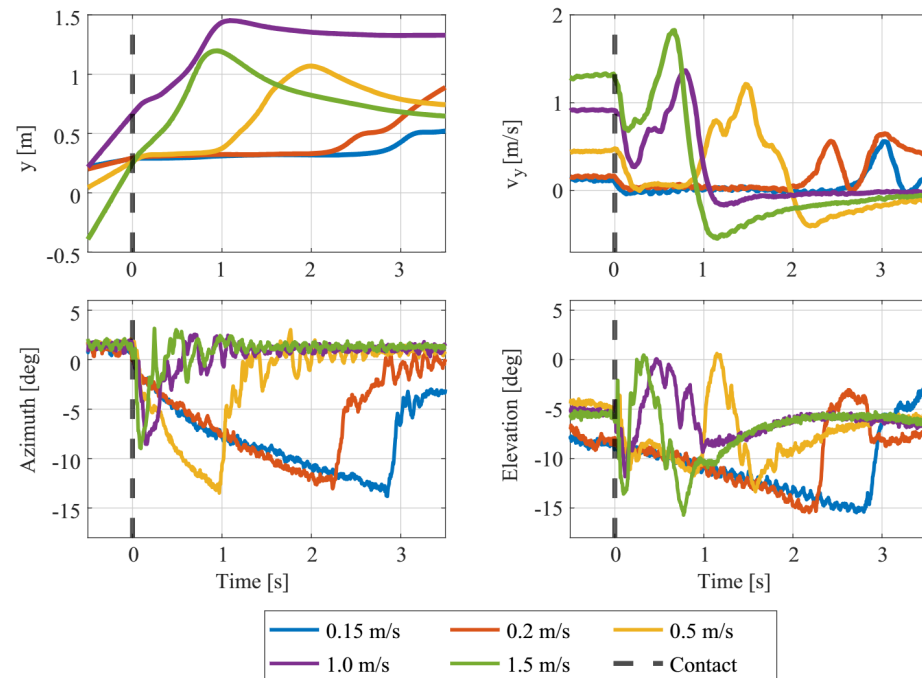


Figure 17. Time series and onboard recorded angle deflections of the minimum speed horizontal squeeze experiment with the first contact point marked. Position on the y-axis, associated velocity, as well as the azimuth and elevation angles of the front right soft arm 0 are depicted. Only arm 0 deflection is plotted for more clear comparison of the effect of approach speed and joint deflection. Note that for slow approaching speeds to the horizontal wedge, the total time spent with bent arms is significantly bigger when compared to high speeds.

introduced in Figure 4a, the propeller frame axes can be calculated from the azimuth and elevation angles, resulting in **Figure 20**. From this figure it can be seen that the angular

deflection presented in Figure 19 during the free flight phase, before coming in contact with the wedge, has minor impact, but during the collision event can cause significant amounts

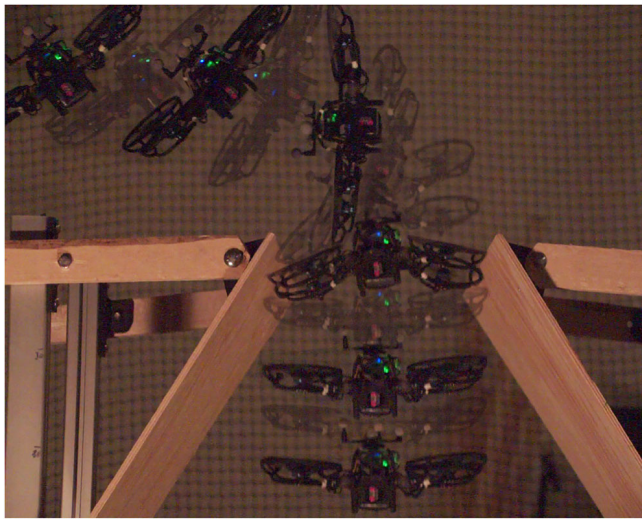


Figure 18. The motion and passive shape adaptation of Morphy evolving during the vertical squeeze experiment. Even with significant attitude perturbation, the system successfully recovered and reached the final waypoint of the commanded trajectory in the yz plane. The system is able to adjust its width W , nominally equal to 25.2 cm, to fit through a wedge of 22.5 cm.

of propeller thrust redirected along body frame x and y axes. More agile flight and prolonged collision events will only serve to increase this effect. This analysis highlights the key role of the 3D Hall-effect sensors for feedback measurements on Morphy and the applicability of the developed adaptive control allocation.

6.6.2. Minimum Speed

Following Section 6.5, the minimum speed required to pass through the vertical wedge is also investigated. Differently from the horizontal wedge experiment, Morphy is not able to pass through the vertical wedge at all speeds. This is shown in **Figure 21** which visualizes select unsuccessful attempts. This is due to the geometry of the structure, as the propeller guards encounter the surface of the wedge and increasing the thrust is insufficient to make the body pass through. For a successful vertical wedge traversal, higher precollision momentum is required such that the velocity does not fall to zero during the in-contact phase. In this specific wedge configuration, as shown in **Figure 19**, it was found that the minimum speed allowing Morphy to pass through the vertical wedge is 3 m s^{-1} .

6.7. Calibration After Collision

Given the elastic nature of the arms, it is of interest to examine the effect of many collisions on the consistency of the joints behavior as well as whether this has a significant impact on the calibration quality. To investigate this, an experiment is conducted where first the front right arm (arm 0) is calibrated, then Morphy is commanded to execute ten collision trajectories as described in Section 6.4, setting the impact speed to 2 m s^{-1} . After executing the collision trajectories, calibration data for arm 0 is again collected. The sequence of collision—recalibration data collection is repeated three times, and the prediction accuracy of the original calibration is evaluated on these, as reported in **Table 6**. From the table one can see limited

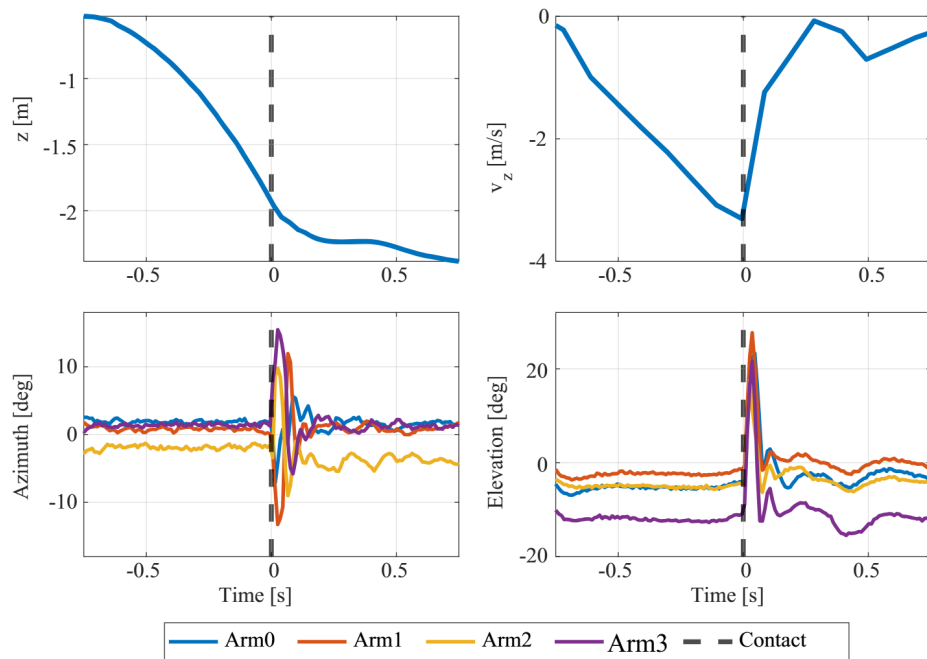


Figure 19. Time series and registered angle deflection of the vertical squeeze experiment with the first contact point marked. Position on the z axis, associated velocity, as well as the azimuth and elevation angles of the four soft arms are depicted.

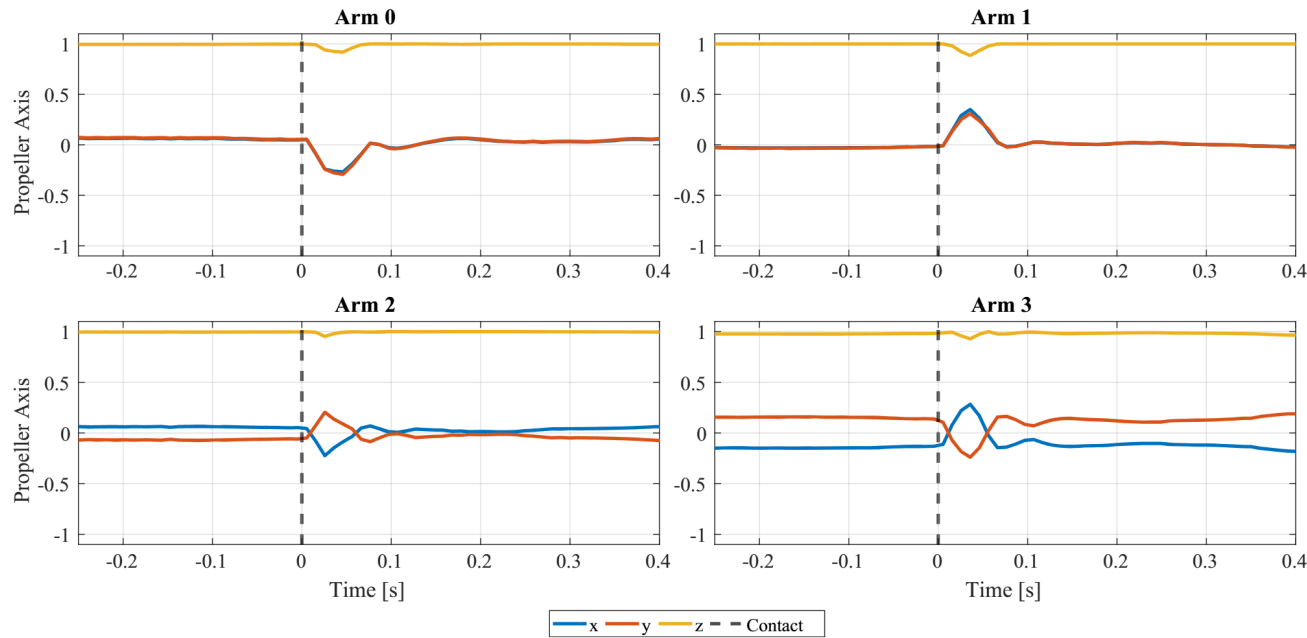


Figure 20. Propeller axes variations, calculated according to Equation (11), as a function of angular deflection related to the vertical wedge traversal experiment presented in Section 6.6 and depicted in Figure 19. Note that during the free flight phase, before contact with the wedge, the impact of the elastic joint and so, of the arms bending, is minimal. However, during the collision event, the bending of the arms can cause a significant amount of propeller thrust to be redirected along the body frame's x and y axes.

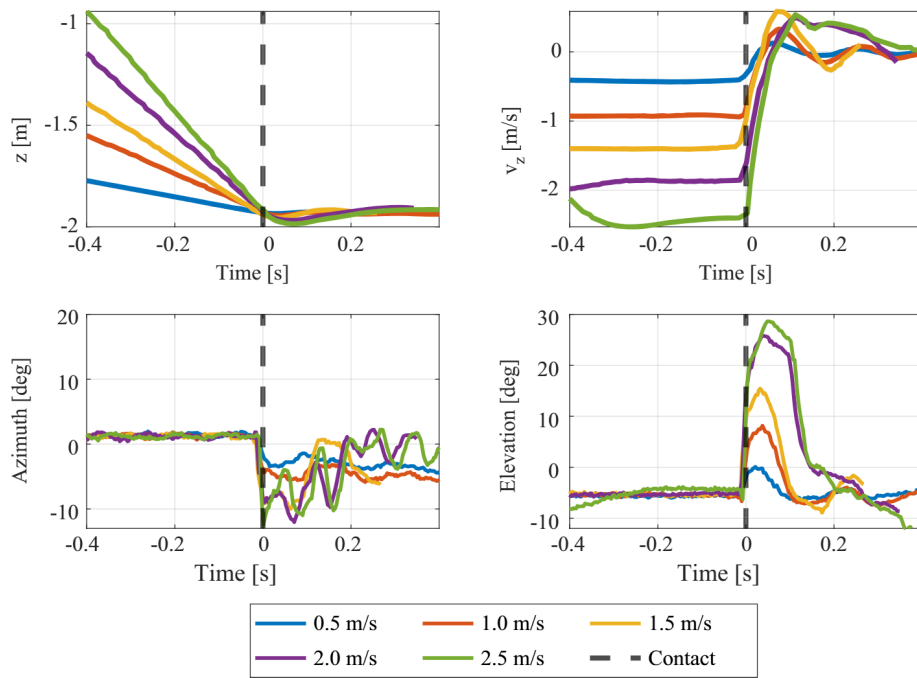


Figure 21. Time series and onboard recorded angle deflections of the minimum speed vertical squeeze experiment, all unsuccessful passages, with the first contact point marked. Position on the z -axis, associated velocity, as well as the azimuth and elevation angles of the front right soft arm arm 0 are depicted. Only arm 0 deflection is plotted for more clear comparison of the effect of approach speed and joint deflection.

variation in the prediction accuracy, likely due to the prototype nature of the robot's construction, but no significant trend of worsening as a function of repeat collisions. Additionally, note that the same calibration is used during all the

aforementioned collision experiments. More refined construction methods will likely benefit the performance in terms of both improved prediction error and durability over repeat collisions.

Table 6. Prediction RMSE of arm 0 calibration from initial dataset evaluated on calibration data gathered post multiple frontal collisions with the obstacle from Section 6.4.

Details	RMSE [deg]	
	Azimuth	Elevation
Initial	1.831	1.260
After 10 Collisions	2.119	1.838
After 20 Collisions	2.473	1.356
After 30 Collisions	2.044	2.588

7. Conclusions and Discussion

This research article presents a novel quadrotor design featuring flexible arm joints integrated with embedded feedback measurements for the arms' motion, alongside collision-tolerance capabilities. The study encompasses the design, modeling and control of the system, followed by a comprehensive analysis of the deflection characteristics of the joints in various scenarios, including free flight, drop tests, and high-speed midflight collisions. Using an adaptive control allocation scheme for thrust and moments, combined with a prevalent P-PID control scheme, the proposed aerial robot demonstrates agile free flight maneuvering, resilience in recovering from collisions, and the ability to navigate through narrow openings by effectively maneuvering through spaces more narrow than its nominal dimensions, both during horizontal and vertical trajectories. Future work shall emphasize three directions, namely 1) the development of high-fidelity parametric models of the joint dynamics and controllers which can leverage such models, 2) utilization of finite-element methods for the detailed study and optimization of the soft joints, as well as 3) autonomous operation based on onboard pose estimation, for example, through visual-inertial fusion.

Appendix A: Control

Note that this section requires additional notation: for an arbitrary vector relating a physical quality of the quadrotor body to the world frame, let $(\cdot)_{\text{ref}}$ denote the setpoint, let $(\hat{\cdot})$ denote the navigation state estimates from the onboard EKF, let $(\cdot)_{\text{ff}}$ denote a feedforward term to the controller, and let $(\cdot)_{\text{lp}}$ denote a low-pass filtered signal. Also, let the error be defined as

$$\Delta(\cdot) = (\cdot)_{\text{ref}} - (\hat{\cdot}) \quad (\text{A1})$$

for an arbitrary vector in Cartesian space, while non-Cartesian elements may demand particular definitions, which will be introduced as necessary. Furthermore, we will use a more concise notation, for example, such that the world-referenced body frame linear velocity v_{WB}^W is instead denoted as v for simplicity of notation. The same simplification will be used for position p , acceleration a , attitude q , and angular velocity ω .

The position controller takes as input the position setpoint p_{ref} , from the trajectory generator, along with the position estimate \hat{p} , and outputs a desired velocity as the result of a P -controller with diagonal gain matrix $K_{P,p}$ following

$$v_{\text{ref}} = v_{\text{ff}} + K_{P,p} \Delta p \quad (\text{A2})$$

where the feedforward term v_{ff} is sourced from the trajectory generator, in the case of differentiable trajectories, for example, position setpoints differentiated with respect to time become velocity setpoints. The velocity setpoint is used as input to the velocity controller which calculates the acceleration setpoint using a PID controller (with diagonal gain matrices $K_{P,v}$, $K_{I,v}$, $K_{D,v}$) by

$$a_{\text{ref}} = a_{\text{ff}} + K_{P,v} \Delta v + K_{I,v} \int \Delta v dt - K_{D,v} \frac{d}{dt} \hat{v}_{\text{lp}} \quad (\text{A3})$$

where, as before, the feedforward term a_{ff} is calculated by the trajectory generator. Since a quadrotor platform is underactuated, the calculated desired acceleration is reinterpreted as a desired roll and pitch tilt such that the $\{B\}$ -frame z -axis aligns with the desired acceleration direction. Thus, the acceleration can be broken down into the desired thrust direction \vec{a}_{ref} and the total acceleration projected along that direction. The total acceleration informs the vertical thrust setpoint, and the pointing direction of the acceleration reference, along with the yaw setpoint ψ_{ref} , from the trajectory generator, determines the desired attitude q_{ref} , following ref. [34].

With the attitude setpoint, we can calculate the attitude error as $\Delta q = \dot{q}^{-1} q_{\text{ref}}$, with error split in real and imaginary parts $\Delta \eta$ and $\Delta \epsilon$, respectively. Thus, we can apply the following nonlinear P -controller^[35]

$$\omega_{\text{ref}} = 2K_{P,q} \text{sign}(\Delta \eta) \Delta \epsilon \quad (\text{A4})$$

with diagonal gain matrix $K_{P,q}$, to calculate the desired angular rate. Finally, given the angular rate setpoint, the angular rate controller is a simple PID controller (with diagonal gain matrices $K_{P,\omega}$, $K_{I,\omega}$, $K_{D,\omega}$) following

$$\mu_{\text{ref}} = K_{P,\omega} \Delta \omega + K_{I,\omega} \int \Delta \omega dt - K_{D,\omega} \frac{d}{dt} \hat{\omega}_{\text{lp}} \quad (\text{A5})$$

resulting in the desired moments.

Supporting Information

Supporting Information is available from the Wiley Online Library or from the author.

Acknowledgements

This material was supported by a) the Research Council of Norway Award NO-321435 and b) the European Commission Horizon project SPEAR (EC 101119774).

Conflict of Interest

The authors declare no conflict of interest.

Author Contributions

Paolo De Petris: Conceptualization: (lead); Formal analysis: (supporting); Investigation: (lead); Methodology: (equal); Software: (supporting); Validation: (equal); Visualization: (equal); Writing—original draft: (equal); Writing—review & editing: (equal). **Morten Nissov:** Formal analysis: (lead); Investigation: (supporting); Methodology: (equal); Software: (lead); Validation: (equal); Visualization: (equal); Writing—original draft: (equal); Writing—review & editing: (equal). **Kostas Alexis:** Conceptualization: (supporting); Investigation: (supporting); Methodology: (supporting); Project administration: (lead); Resources: (lead); Validation: (supporting); Writing—original draft: (supporting); Writing—review & editing: (supporting).

Data Availability Statement

The data that support the findings of this study are available from the corresponding author upon reasonable request.

Keywords

aerial robots, collision tolerances, soft mechanisms

Received: June 14, 2024

Revised: September 3, 2024

Published online:

- [1] Y. Ma, J. G. Ning, H. L. Ren, P. F. Zhang, H. Y. Zhao, *J. Exp. Biol.* **2015**, 218, 2136.
- [2] A. M. Mountcastle, S. A. Combes, *J. Exp. Biol.* **2014**, 217, 1108.
- [3] P. Henningsson, *R. Soc. Open Sci.* **2021**, 8, 211072.
- [4] M. A. Badger, K. McClain, A. Smiley, J. Ye, R. Dudley, *J. Exp. Biol.* **2023**, 226, jeb245643.
- [5] P. De Petris, S. J. Carlson, C. Papachristos, K. Alexis, *arXiv:2212.03196*, **2022**.
- [6] A. Klaptocz, A. Briod, L. Daler, J.-C. Zufferey, D. Floreano, in *2013 IEEE/RSJ Int. Conf. on Intelligent Robots and Systems*, IEEE, Piscataway, NJ **2013**, pp. 1886–1892.
- [7] S. Mintchev, S. de Rivaz, D. Floreano, *IEEE Robot. Autom. Lett.* **2017**, 2, 1248.
- [8] K. Patnaik, S. Mishra, S. M. R. Sorkhabadi, W. Zhang, in *2020 IEEE/RSJ Int. Conf. on Intelligent Robots and Systems (IROS)*, IEEE, Piscataway, NJ **2020**, pp. 1364–1370.
- [9] R. de Azambuja, H. Fouad, G. Beltrame, *arXiv:2107.11090*, **2021**.
- [10] R. de Azambuja, H. Fouad, Y. Bouteiller, C. Sol, G. Beltrame, *arXiv:2103.04423*, **2021**.
- [11] J. Zha, X. Wu, R. Dimick, M. W. Mueller, in *IEEE/ASME Transactions on Mechatronics*, IEEE, Piscataway, NJ **2024**.
- [12] P. De Petris, H. Nguyen, M. Kulkarni, F. Mascarich, K. Alexis, in *2021 IEEE Int. Conf. on Robotics and Automation (ICRA)*, IEEE, Piscataway, NJ **2021**, pp. 2286–2292.
- [13] A. Fabris, S. Kirchgeorg, S. Mintchev, in *2021 IEEE Int. Symp. on Safety, Security, and Rescue Robotics (SSRR)*, IEEE, Piscataway, NJ **2021**, pp. 48–54.
- [14] A. Fabris, E. Aucone, S. Mintchev, *Adv. Intell. Syst.* **2022**, 4, 2200113.
- [15] S. T. Bui, Q. K. Luu, D. Q. Nguyen, N. D. M. Le, G. Loianno, V. A. Ho, *arXiv:2202.07177*, **2022**.
- [16] E. Aucone, C. Geckeler, D. Morra, L. Pallottino, S. Mintchev, *Nat. Commun.* **2024**, 15, 2646.
- [17] D. Floreano, S. Mintchev, J. Shintake, in *Bioinspiration, Biomimetics, And Bioreplication 2017*, Vol. 10162, SPIE, Bellingham, WA **2017**, p. 1016203.
- [18] A. Desbiez, F. Expert, M. Boyron, J. Diperi, S. Viollet, F. Ruffier, in *2017 Workshop on Research, Education and Development of Unmanned Aerial Systems (RED-UAS)*, IEEE, Bellingham, WA **2017**, pp. 222–227.
- [19] D. Falanga, K. Kleber, S. Mintchev, D. Floreano, D. Scaramuzza, *IEEE Robot. Autom. Lett.* **2018**, 4, 209.
- [20] V. Riviere, A. Manecy, S. Viollet, *Soft Robot.* **2018**, 5, 541.
- [21] T. Tothong, J. Samawi, A. Govalkar, K. George, in *2020 11th IEEE Annual Information Technology, Electronics and Mobile Communication Conf. (IEMCON)*, IEEE, Bellingham, WA **2020**, pp. 0589–0596.
- [22] N. Bucki, J. Tang, M. W. Mueller, *IEEE Trans. Robot.* **2022**, 39, 539.
- [23] F. Stella, J. Hughes, *Front. Robot. AI* **2023**, 9, 1059026.
- [24] P. H. Nguyen, M. Kovač, in *IOP Conference Series: Materials Science And Engineering*, vol. 1261, IOP Publishing, Bristol, UK **2022**, p. 012006.
- [25] F. Ruiz, B. C. Arrue, A. Ollero, *IEEE Robot. Autom. Lett.* **2022**, 7, 11086.
- [26] J. Haluška, J. Västanälvy, A. Papadimitriou, G. Nikolakopoulos, in *2022 30th Mediterranean Conf. on Control and Automation (MED)*, IEEE, Piscataway, NJ **2022**, pp. 475–480.
- [27] A. Fabris, K. Kleber, D. Falanga, D. Scaramuzza, in *2021 IEEE Int. Conf. on Robotics and Automation (ICRA)*, IEEE, Piscataway, NJ **2021**, pp. 592–598.
- [28] Formlabs Elastic 50A Resin V2, <https://formlabs-media.formlabs.com/datasheets/2401869-TDS-ENUS.pdf>, (accessed: May 2024).
- [29] PMD Technologies, <https://pmdtec.com/en/technology/time-of-flight/>, (accessed: May 2024).
- [30] OV Omnivision, <https://www.ovt.com/products/ov7251/>, (accessed: May 2024).
- [31] TDK Invensense, <https://invensense.tdk.com/download-pdf/icm-42688-p-datasheet/>, (accessed: May 2024).
- [32] TMAG5273 Low-Power Linear 3D Hall-Effect Sensor with I₂C Interface, <https://www.ti.com/lit/ds/symlink/tmag5273.pdf>, (accessed: May 2024).
- [33] L. Meier, D. Honegger, M. Pollefeyns, in *2015 IEEE Int. Conf. on Robotics and Automation (ICRA)*, IEEE, Piscataway, NJ **2015**, pp. 6235–6240.
- [34] L. Meier, D. Agar, B. Küng, J. Oes, T. Gubler, M. Grob, P. Riseborough, R. Bapst, A. Babushkin, D. Sidrane, M. Bresciani, px4dev, S. Fuhrer, M. Charlebois, J. Goppert, N. Marques, A. D. Antener, D. Mannhart, P. B. Bot, kritz, M. Whitehorn, K. Mohammed, J. Lim, P. van der Perk, S. Wilks, M. Sauder, P. Kirienko, S. Smeets, M. Rivizzigno, H. Willee, Px4/px4-autopilot: v1.14.3, **2024**. <https://doi.org/10.5281/zenodo.11288850>.
- [35] D. Brescianini, M. Hehn, R. D'Andrea, Nonlinear Quadrocopter Attitude Control: Technical Report, **2013**, <http://hdl.handle.net/20.500.11850/154099>, (accessed: November 2024).